International Journal of Thermophysics (2020) 41:42
https://doi.org/10.1007/s10765-020-2618-x

TEMPMEKO 2019

Thermodynamic Temperature Measurements from the Triple Point of Water up to the Melting Point of Gallium

J. V. Widiatmo[1] · T. Misawa[1] · T. Nakano[1] · I. Saito[1]

Received: 30 September 2019 / Accepted: 5 February 2020 / Published online: 21 February 2020
© Springer Science+Business Media, LLC, part of Springer Nature 2020

Abstract

A new acoustic gas thermometry (AGT) system, which introduces a 1-L quasi-spherical resonator (QSR) made of oxygen-free copper, was built at the National Metrology Institute of Japan (NMIJ/AIST). The inner surface of the new QSR was machined using a diamond-turn tool. Improvement in the pressure measurement was introduced to allow direct measurement of the gas pressure in the resonator. The new AGT system was evaluated based on the measurement of the speed of sound in argon at the triple point of water and the melting point of gallium under the pressure range from 700 kPa down to 50 kPa. Based on these speed of sound measurements, the thermodynamic temperatures at the melting point of gallium were determined. The speed of sound measurements at isotherms of 283.15 K and 293.15 K were also conducted, and the related thermodynamic temperatures were determined. Based on the measured thermodynamic temperature T, the values of difference between T and the temperature T_{90} based on the International Temperature Scale of 1990 (ITS-90), $(T-T_{90})$, along with the associated uncertainties, were calculated. The $(T-T_{90})$ obtained in the present work were 1.3 ± 0.7 mK, 2.7 ± 0.8 mK, and 4.1 ± 0.8 mK for T_{90} of 283.15 K, 293.15 K, and 302.9146 K, respectively. These values were found to be in agreement within the estimated uncertainty with the currently reported values that exist in temperature range overlapping with the present work.

Keywords Acoustic gas thermometry · Acoustic resonance · Boltzmann constant · Microwave resonance · Primary thermometry

Selected Papers of the 14th International Symposium onTemperature and Thermal Measurements in Industry and Science.

✉ J. V. Widiatmo
janu-widiatmo@aist.go.jp

[1] National Metrology Institute of Japan, AIST, Tsukuba, Japan

1 Introduction

In May 2019, new definition of some base units of the International System of Units (SI) has been effective by fixing the numerical values of fundamental constants [1]. For thermodynamic temperature, the unit kelvin has come to be defined based on the Boltzmann constant. Acoustic gas thermometry (AGT) is one of the methods for measuring thermodynamic temperature, which utilizes the dependence of the speed of sound on thermodynamic temperature in a dilute gas. Moldover et al. [2] first reported in detail the development of a spherical acoustic resonator for the speed of sound measurement in argon, and determined the Boltzmann constant based on measurements at the triple point of water. Since in principle, based on the fixed Boltzmann constant, the AGT can accurately measure the thermodynamic temperature, it was then also applied for thermodynamic temperature measurements [3–10]. Recent reports consistently evidenced systematic differences between thermodynamic temperature T and the temperature T_{90} based on the International Temperature Scale of 1990 (ITS-90) [11]. Since the International Temperature Scale was defined in 1990 as the best approximation to thermodynamic temperature at that time, the evaluation of the difference $(T-T_{90})$ by using state-of-the-art technique becomes important to improve practical temperature measurements based on the ITS-90 [12].

Taking into account the importance of thermodynamic temperature measurement, we built a new AGT system at the National Metrology Institute of Japan (NMIJ). This new system is a continuation of our work on developing a prototype acoustic gas thermometry (AGT) system, as already reported elsewhere [13]. The new AGT system introduces a 1-L quasi-spherical resonator (QSR) made of oxygen-free copper (OFC) fabricated using a diamond-turn finishing of its internal surface. A new mounting configuration of the resonator, intended to reduce the deformation caused by the suspension of the cavity under its own weight, was evaluated by relative measurements of the thermodynamic temperature based on the ratio of speed of sound at several temperatures.

In the following sections, we report about the design and the construction of our new AGT system including the improvement of the performance, which was achieved compared to our earlier system. We also consider two different QSR assemblies, and the corresponding measured thermodynamic temperatures as well as their measurement uncertainty are evaluated. The comparison of the results with the previous existing determinations of $(T-T_{90})$ at the overlapping temperature range are also evaluated.

2 Measurement Apparatus

The AGT system developed in this work consists of a QSR, a gas-handling system, an acoustic measurement system, and a microwave measurement system. The set-up of the AGT system is shown schematically in Fig. 1. Each part is described in the following subsections.

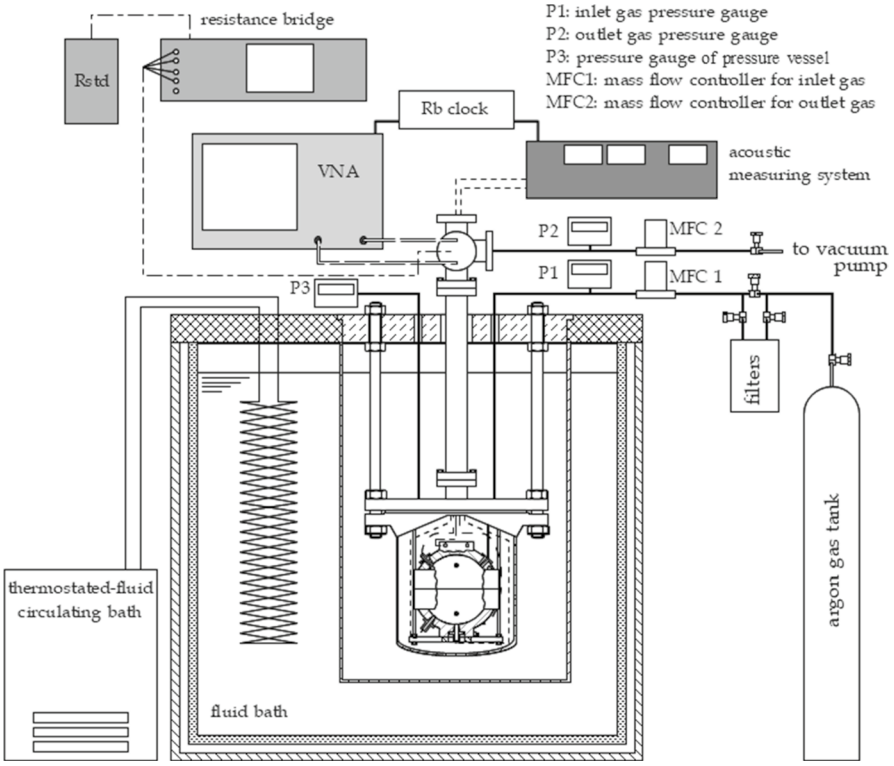

Fig. 1 Measurement system set-up

2.1 Resonator

The resonator developed in this work was an assembly of two half quasi-spheres, each made of oxygen-free copper by employing a diamond-turn tool. The inner shape of the QSR was designed to be an ellipsoid as expressed by the following equation, where a is the nominal radius, and ϵ_1 and ϵ_2 are the deformation parameters.

$$\frac{x^2}{a^2\left(1+\epsilon_1\right)^2}+\frac{y^2}{a^2}+\frac{z^2}{a^2\left(1+\epsilon_2\right)^2}=1. \tag{1}$$

The QSR is illustrated in Fig. 2. The nominal values of a, ϵ_1, and ϵ_2 are 62 mm, 0.0005, and 0.001, respectively, and the wall thickness of the QSR is 15 mm. These specifications were the same as in the design by Underwood et al. [14]. The equatorial part of the QSR was made like a belt shape, where stainless steel bolts for aligning and fixing the hemispheres, and capsule-type standard platinum resistance thermometers (cSPRTs) were placed. Six ports through the wall of the QSR were made to accommodate OFC plugs used to hold two microphones, two antennas, and two tubes allowing gas to flow through. The plug for transmitter microphones was set at

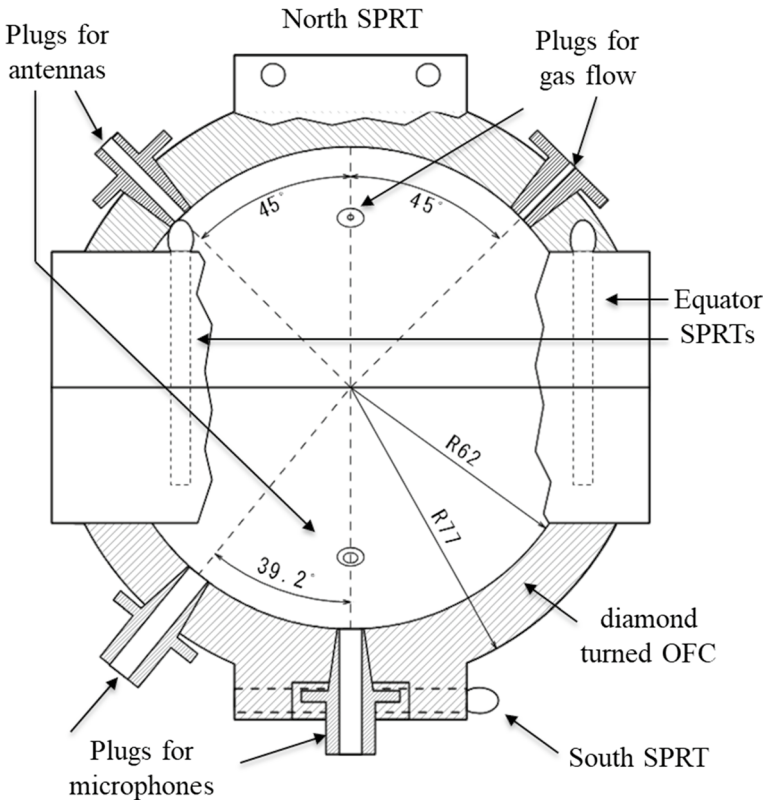

Fig. 2 Quasi-spherical resonator

angle 39.2° from the plug for receiver microphones set on the south end. This setting was following the design proposed by Mehl et al. [15] in order to have the best possible separation of (0,2) acoustic radial mode from the neighboring (3,1) acoustic non-radial mode. Plugs for gas-flowing tubes were set on the upper (or north) hemisphere at angular position 45° from the north end. One port for an antenna was placed in the upper hemisphere at the angle position 45° from north end, and one port for another antenna in the lower hemisphere at the angle position 45° from the south end. In the north end, two holes were drilled as housing of cSPRTs. The same holes were also made in the south end.

The QSR was enclosed in a stainless steel pressure vessel by fixing it to the cap of the vessel with three rods. Figure 3 illustrates two alternative fixing configurations that were evaluated in this work. In the first configuration, shown in Fig. 3a, an OFC circular plate was fixed to the lower surface of the belt-shaped equator, and three stainless steel long bolts (6 mm OD) connected the plate to the pressure vessel cap. In this configuration, as shown in Fig. 3a, the QSR was in the 'hung at the equator' position (called hereafter the 'hung' position). Small heaters (Sakaguchi E.H VOC, MS-3, 10×10 mm, max 40 W) for controlling the temperature of the QSR

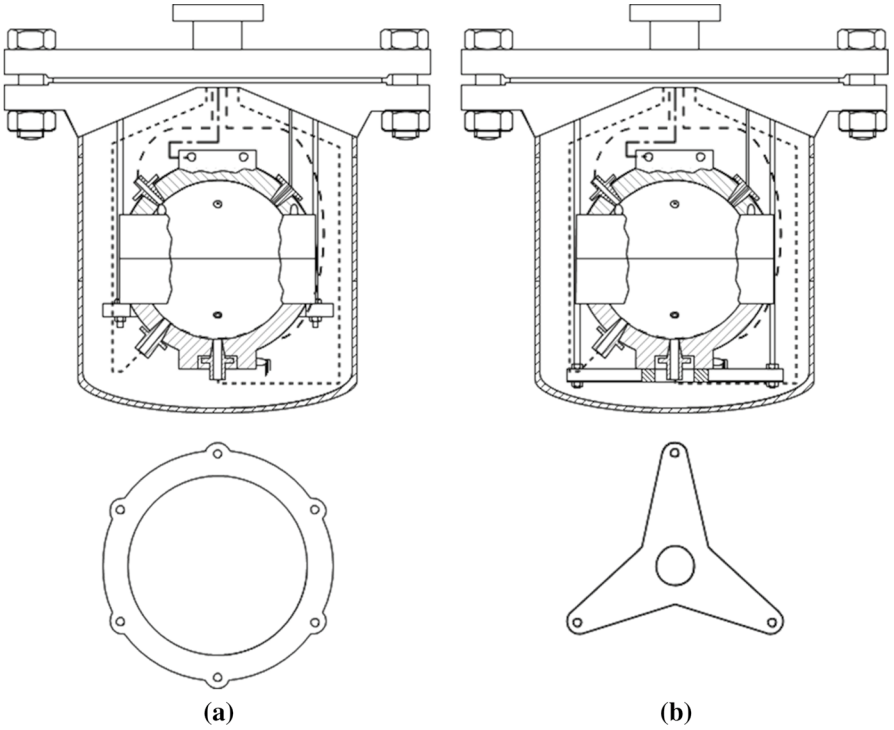

Fig. 3 Fixing configuration of the resonator (up) and fixing plate (down): (**a**) 'Hung' configuration, (**b**) 'Sit' configuration

were attached on the surface of the circular plate and the fixing rods. In the second configuration, shown in Fig. 3b, an OFC made star-shaped plate was fixed on the flat surface at the south end of the QSR, and three OFC rods (15 mm OD) connected the plate to the pressure vessel cap. In this configuration, the QSR was in the 'sit on plate' position (called hereafter the 'sit' position). A small heater (Sakaguchi E.H VOC, MS-M5, 5 ×5 mm, max 15 W) was attached on each rod.

2.2 Gas System

A gas-handling system was built to maintain argon gas flowing through the QSR, as an attempt to minimize the effect of impurities from outgassing. Two argon gas samples of 99.9999 % purity (Japan Fine Product, G1) were used. All tubes used in the gas-handling system were made of electro-polished stainless steel. The inlet and outlet tubes connected directly to the gas port of the QSR were 1/16-in. nickel tube with length of 1.1 m. A filter for reducing oxygen content (Nikka Seiko, GC-RX) and a filter for reducing water content (Nikka Seiko, DC-A4) were installed in the upstream side of the gas-handling system. Two mass flow controllers (MFC, Fujikin, FCST1005MZFC) were used to set a constant desired flow rate. Flow rates for both

mass flow controllers fixed at 2 sccm for the 'hung' position and 5 sccm for the 'sit' position were used in this work. One was installed in the upstream side (MFC1), while the other in the downstream side (MFC2). A pressure gauge (Paroscientific, Model 745, max 1.4 MPa) was installed in the upstream side (identified as P1) and the same model pressure gauge was in the downstream side (identified as P2). Before being installed in the handling system, the pressure gauge P2 was calibrated in the range up to 700 kPa by the Pressure Standard Laboratory at NMIJ/AIST, while the pressure gauge P1 was calibrated by comparison with the pressure gauge P2. A third pressure gauge (Paroscientific, Model 2100A, max 700 kPa, identified as P3) was introduced and also calibrated by comparison with the pressure gauge P2. The pressure gauge P3 was once installed at the entrance of the gas line into the liquid bath (62 cm above the gas inlet into the QSR) in order to measure the gas pressure at this point under the flow rate of 2 sccm and 5 sccm. The relation between the pressure P3 the pressure P1 is shown in Fig. 4, implying that the effect of the flow on the indicated pressure is small. The pressure gauge P3 was then removed from the upstream gas line and directly connected to the pressure vessel (62 cm above the gas outlet from the QSR). The installation of the pressure gauge P3 here was intended to measure pressure inside the pressure vessel. The pressure head and the pressure drop induced by the gas flow, which was calculated based on the Hagen–Poiseuille law, were added as corrections to the pressure measured by pressure gauges P1 and P3, to have an average value of pressure inside the QSR.

2.3 Temperature Measurement System

The temperature of the QSR was measured by employing four cSPRTs. As shown in Fig. 2, one cSPRT was placed at the north end, one at the south end, and two around the equator. The cSPRT at the south end was Fluke 5686-B (S/N HS225), and the rest cSPRTs were Chino R800-0 (S/N RS913-2, RS143-02, and RS143-03). These

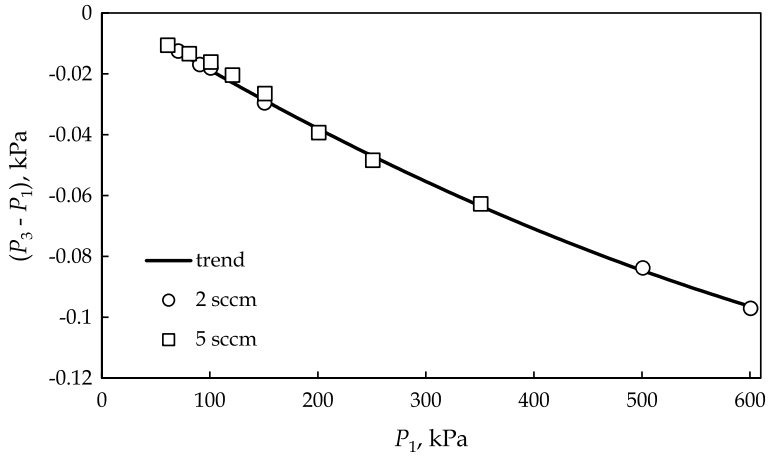

Fig. 4 Pressure difference under gas flow

cSPRTs were calibrated before use at the triple point of water and the triple point of gallium (302.9166 K). Three of them (HS225, RS913-2, and RS143-03) were additionally calibrated at the triple point of mercury (234.3156 K) and the triple point of argon (83.8058 K). Two of them (HS225 and RS913-2) have been used for a long time since our earlier work [13], the stability of which was evaluated using the maintenance system in NMIJ/AIST [16] to estimate a maximum long-term change within ± 0.15 mK. The measurement of the resistance of the cSPRTs in this work was conducted by employing a resistance measuring device (Fluke, 1595A Super-Thermometer) coupled with a temperature-controlled 100-ohm standard resistor (Tinsley, 5685A). The resistance measurements for cSPRTs were compensated for the self-heating effect. For maintaining the temperature of the QSR, the temperature at the south end was used as the reference point.

2.4 Microwave Measurement System

Speed of sound measurements in the QSR require an accurate value of the radius of the QSR. To obtain this value at various temperatures and pressures, the microwave resonance method [7] was adopted in this work. The microwave measurement was conducted by employing two loop antennas, each of which was fixed to the related plug using an epoxy adhesive (stycast) that filled the gap between tip part of the antenna and the plug, as described in earlier report [13]. These antennas were connected to a vector network analyzer (Agilent Technology, ENA5071C) by coaxial cables through hermetic connectors. The vector network analyzer was synchronized to a rubidium clock (Stanford Research Systems, FS725), which served as frequency reference.

2.5 Acoustic Measurement System

Speed of sound measurements in argon within the QSR were performed by employing two free-field externally polarized microphones (G. R. A. S., 40BF), whose diameter was 1/4 in.: one for exciting and one for detecting the acoustic field. A preamplifier (G. R. A. S., 26AC) was directly connected to the receiver microphone. A signal generator (Agilent Technology, 33220A) was employed for generating sinusoidal signals. The signal generator referred to the same rubidium clock as the vector network analyzer so that the ratio between the acoustic and microwave frequency measurement could be accurate. An actuator amplifier (G. R. A. S., 14AA) amplified and provided this signal to the source microphone. Then the transmitted signal was detected by the receiver microphone and amplified by the conditioning amplifier (Brüel and Kjær, 2690 OS1). A lock-in amplifier (Stanford Research Systems, SR830) was used to measure the signal detected by the receiver microphone.

2.6 Measurement Set-up and Procedures

As illustrated in Fig. 1, the QSR was enclosed in the pressure vessel. The pressure vessel was immersed in a liquid bath, which maintains a temperature slightly lower

than that to measure. As aforementioned in Sect. 2.1, small heaters were employed to adjust the temperature of the QSR to the target temperature. A liquid-circulating chiller (Julabo, FP50) was used to adjust the temperature of the liquid bath. Four cylindrical rods hold the pressure vessel at the cap plate of the liquid bath. The pressure vessel was surrounded by an aluminum basket with a punched wall, so that the effect from liquid flow was minimized. A connection tube was used as a feedthrough of the cables. A vacuum pump was employed to pump out the argon gas for realizing a continuous flow.

In this work, thermodynamic temperature was determined by implementing the method of relative acoustic gas thermometry, which is based on the evaluation of the ratio between the speed of sound at the temperature T of interest and the speed of sound at TPW [3, 4]. We adopted 273.16 K as the value of the TPW and 0.1 mK as its standard uncertainty on the basis of the Appendix 2 of SI Brochure—9th edition [17]. The measurements at the TPW were conducted at first, preceding those at other temperatures. For one isotherm, microwave resonance frequencies (based on the S-parameter S_{21}) were first measured under vacuum, then series of the microwave and the acoustic resonance frequency were measured at pressures from 700 kPa down to 50 kPa, and terminated by measurement of the microwave resonance frequencies under vacuum. At each pressure, a series of acoustic and microwave resonance frequency measurements were repeated three times. In one series, the acoustic resonance frequencies for radial modes (0,n) with $n=2$ to 8 were measured, and the microwave resonance frequency for transverse magnetic modes TM1l and transverse electric modes TE1k with $l=1$ to 4 and $k=1$ to 3.

At first, the abovementioned procedures were done with the QSR in the 'hung' configuration at the TPW and the melting point of gallium. The argon gas used in the first trial was identified as Sample 1 in this work. The QSR configuration was then made to the 'sit' configuration described in Sect. 2.1. The change in the QSR configuration was performed very carefully so that changes in the QSR alignment, plugs, and tubes position were minimized. We needed, however, to remove temporarily the receiver microphone at the south-end when installing the star-shaped plate (see Sect. 2.1). The microphone was reinstalled to the same port with the original condition. The same measurement procedures were then executed with the QSR in the 'sit' configuration at the TPW, 283.15 K, 293.15 K, and the melting point of gallium. The argon gas used in this 'sit' configuration was different from that at the 'hung' configuration, and was identified as Sample 2.

3 Measurement Results

3.1 Microwave Measurement

The measured microwave frequencies at each TM or TE mode were fitted to the resonance function reported in [18] introducing linear and quadrature backgrounds to have three resonance frequencies and their half-widths for each mode. These resonance frequencies were then corrected for the effects from the microwave penetration length [18] and from the waveguide [14]. The second-order shape correction

proposed by Mehl [19] was applied to derive the deformation parameters, ϵ_1 and ϵ_2 in Eq. 1, as well as the nominal radius of the QSR, a. The values of the refractive index of argon used for these derivations were calculated using the method in [18] (Eq. 15 truncated after the second term). From values a obtained at various temperatures and pressures, the nominal radius of the QSR can be expressed by the following relation [20].

$$a(T,P) = a_0\left[1 - \frac{K_P}{3}P + (T - 273.16)K_T\right], \tag{2}$$

where K_P and K_T in Eq. 2 were empirically determined as the slopes of the dependence of a on pressure P and temperature, respectively. These may refer to isothermal compressibility and thermal expansion coefficient of the QSR, respectively. The values of K_P in Eq. 2 at the TPW were 1.05×10^{-11} Pa^{-1}, while K_T was 1.66×10^{-5} K^{-1}. a_0 in Eq. 2 represents the nominal radius of the QSR at $T=273.16$ K and zero pressure, which was the average of the extrapolated values at $P=0$ of mode TM12 to TM14 and TE11 to TE13, as shown in Fig. 5 by a dotted line for 'hung' configuration and a dashed line for 'sit' configuration. The discrepancy in a_0 between the two configurations was 1.2 ppm. In both configurations, inconsistency of mode TM11 was estimated to be 2.6 ppm. The deformation parameters ϵ_1 and ϵ_2 obtained from the microwave measurements at various modes are summarized in Fig. 6, where a slight discrepancy was observed between the 'hung' and 'sit' condition. We found that ϵ_1 and ϵ_2 were significantly smaller than designed. It is likely that this leads to an imperfect lift of the threefold degeneracy of TM1l and TE1k modes, whose triplet peaks appeared in a narrow range of frequency, f, as shown in Fig. 7, where the vertical axis is S_{21} parameter.

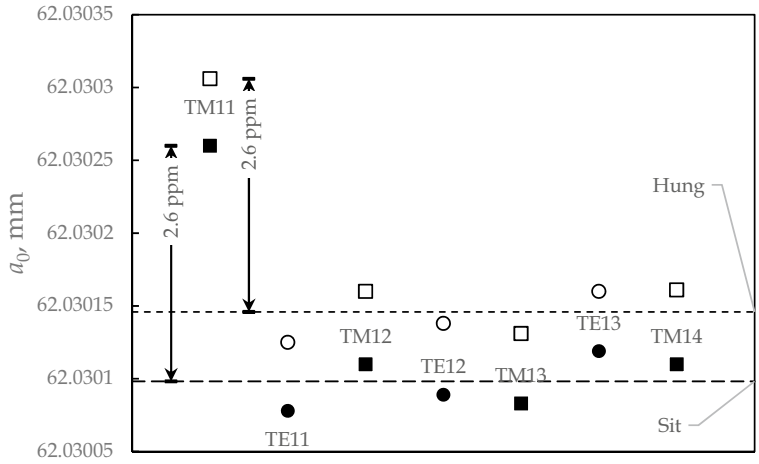

Fig. 5 Effective radius of the resonator for various modes

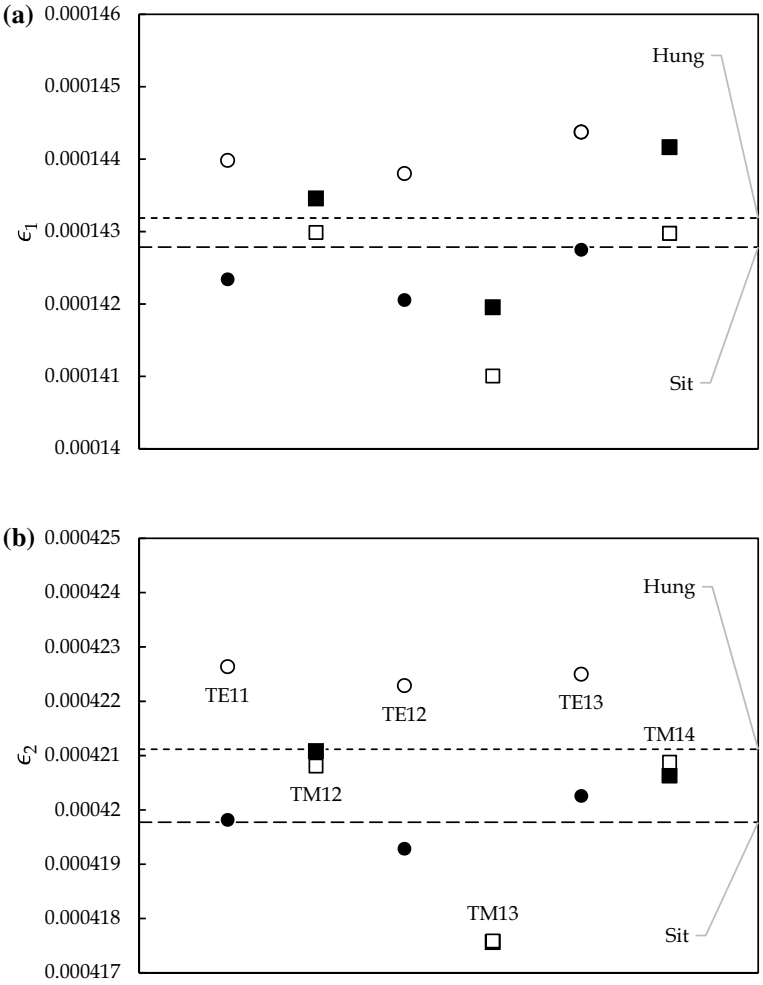

Fig. 6 Deformation parameters of resonator for various modes: (**a**) ϵ_1, (**b**) ϵ_1

3.2 Acoustic Measurement

In the 'hung' position, the resonance frequencies of several acoustic modes were measured at pressures from 700 kPa down to 50 kPa at the TPW, and from 500 kPa down to 60 kPa at the melting point of gallium. In the 'sit' configuration, on the other hand, the measurements at all isotherms were performed in the pressure range from 500 kPa down to 60 kPa. The measured acoustic frequencies at each radial mode were fitted to the resonance function reported in [18] by introducing linear background to derive the resonance frequency and its half-width for each mode. The derived resonance frequencies were corrected for the effects from the thermal boundary layer and the acoustic transducer perturbation following the method compiled in [18]. The thermal accommodation coefficient, h, was assumed as $h=1$ for

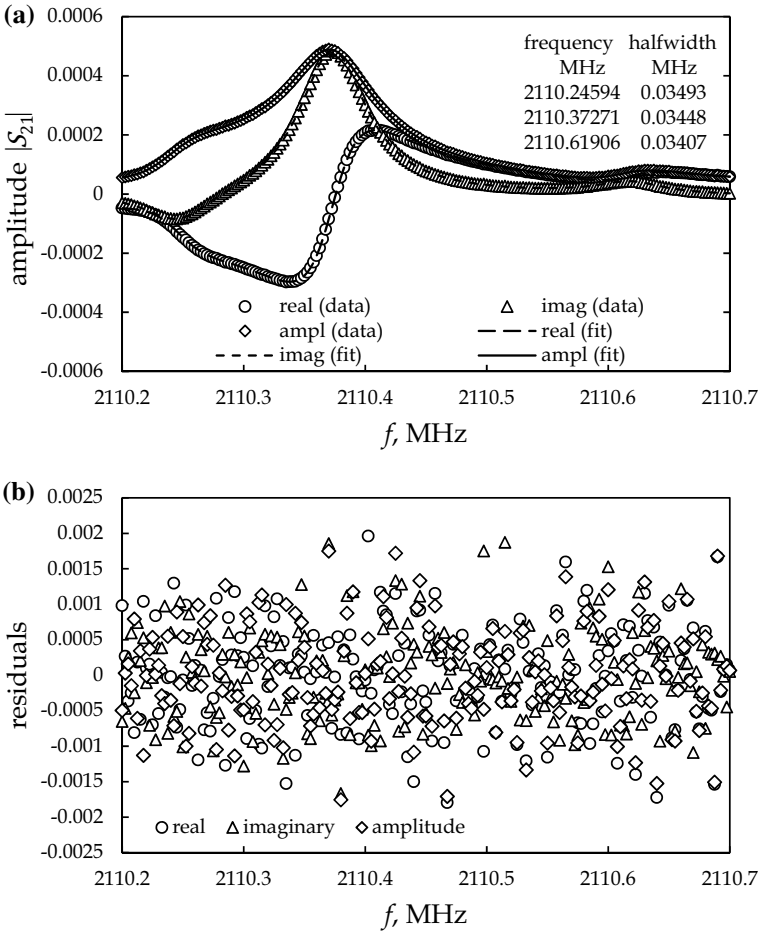

Fig. 7 Microwave resonance at mode TM11: (**a**) measured data and correlation, (**b**) residuals of the fit

the thermal boundary correction here [6]. They were also corrected for the duct perturbation coming from the inlet and outlet gas tubes, by employing the model proposed by Gillis et al. [15, 21].

Contribution of the thermal boundary layer and bulk dissipation to the resonance half-width were calculated following [18], and the calculation for the contribution of the inlet and outlet gas tubes to the resonance half-width was following [15]. The difference between the frequency half-width and the above-calculated contributions, which is called the excess half-width hereafter, is depicted in Fig. 8. It is obvious from Fig. 8 that at frequencies around 14 kHz, the excess half-width, especially at the TPW, became quite large. This frequency was near the acoustic mode (0,6). This large excess half-width is related to the existence of resonance frequency of the QSR itself, which is often called the breathing frequency of the QSR, f_{br}. This frequency should be determined and compensated for. Moldover et al. [3] derived a method to

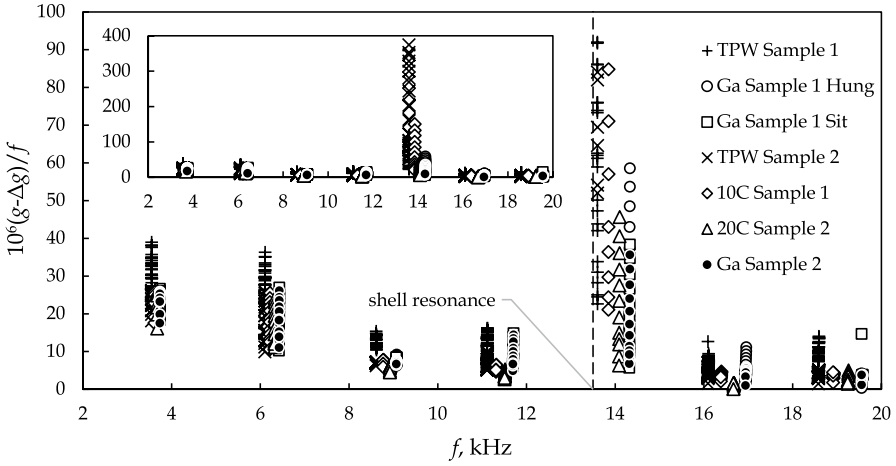

Fig. 8 Excess half-width of acoustic resonance for various modes, inset for whole scale

determine the breathing frequency using only the properties of the material of the QSR. When this method was applied to our QSR, the f_{br} was 15.2 kHz, which was not near the mode (0,6), which was around 13.6 kHz. Pitre et al. [22] proposed a method for determining f_{br} by optimizing the acoustic frequency that produces second acoustic virial coefficient independent on the observed radial modes, and in this work, this strategy was adopted. The speed of sound, w, was derived from the resonance frequency, by introducing a and K_P determined from the microwave resonance frequencies measured at the respective isotherms for mode TM12 to TM14 and TE11 to TE13. The speed of sound measured at the TPW for modes (0,2) to (0,8), with exception of the mode (0,6), was fitted to the following equations, A_0 to A_2 are the fitting parameters, and A_3 is 1.45×10^{-9} $\mathrm{m^2{\cdot}s^{-2}{\cdot}kPa^{-3}}$ for the TPW as reported in [3, 6].

$$w^2 - \mathrm{A}_3P^3 = \mathrm{A}_0 + \mathrm{A}_1P + \mathrm{A}_2P^2 \tag{3}$$

$$w = \frac{2\pi a}{Z_{0,n}}\left(f_{0,n} - \Delta f\right). \tag{4}$$

Δf is the sum of corrections to the unperturbed resonance frequency $f_{0,n}$, and $Z_{0,n}$ is the eigenvalue of acoustic mode $(0,n)$. The following correction for the resonance frequency due to the shell effect is adopted [22], where ρ_{wall} and w_{wall} are the density of and the speed of sound in the resonator material (copper), and t is the thickness of the wall of the resonator.

$$\frac{\Delta f_{\mathrm{sh}}}{f_{0,n}} = \frac{5a}{6t\rho_{\mathrm{wall}}w_{\mathrm{wall}}^2}\frac{1}{1-\left(\frac{f_{0,n}}{f_{\mathrm{br}}}\right)^2}. \tag{5}$$

Adopting the method proposed in [22] gives the value of f_{br} to be 13.5 kHz. This value is shown in Fig. 8 as a vertical broken line.

The speed of sound obtained at the TPW, 283.15 K, 293.15 K, and the melting point of gallium, after the correction of resonance frequency described above, was fitted to Eq. 3 to obtain the value of A_0, which corresponds to the square of the speed of sound at the limit condition of $P=0$, w_0^2. For fitting the data at the TPW, the value of A_3 reported in [3, 6] was introduced. For the other temperatures, value of A_3 was obtained from quadratic fitting of those reported in [23] to obtain the values of 1.09×10^{-9}, 7.9×10^{-10}, and 5.4×10^{-10} $m^2{\cdot}s^{-2}{\cdot}kPa^{-3}$ for 283.15 K, 293.15 K, and 302.9146 K, respectively. Figure 9 summarizes the obtained data, w, from Eq. 3, w_{corr}, for selected modes and configurations at aforementioned temperatures. Most of the data agreed with Eq. 3 within ±2 ppm, except those at lower pressures below 150 kPa, which showed a large scatter. At a dilute gas condition, electrical noise occurred more frequently than at a dense gas condition, and the determination of the resonance frequency became erratic. For the mode (0,2) at the TPW, as shown in Fig. 9a, c, even at higher pressures the scatter was larger than ±2 ppm. This may be caused by the effect from the neighboring non-radial mode (3,1) (see [3]), which was not completely suppressed by the present system.

3.3 Discussion

From the speed of sound extrapolated to the limit $P=0$ described above, the thermodynamic temperature, T, was determined by employing the following relationship.

$$T = T_{\mathrm{ref}}\frac{\lim\limits_{P\to0} w^2(P,T)}{\lim\limits_{P\to0} w^2\left(P,T_{\mathrm{ref}}\right)} = T_{\mathrm{ref}}\frac{w_0^2(T)}{w_0^2\left(T_{\mathrm{ref}}\right)}. \tag{4}$$

As T_{ref}, we adopted the TPW, that $T_{ref}=273.16$ K, the value based on the Appendix 2 of SI Brochure—9th edition [17], and its uncertainty was 0.1 mK, corresponding to a relative uncertainty 3.7×10^{-7} [17, 24]. Figure 10 represents temperatures calculated using Eq. 4 for four isotherms based on the speed of sound obtained by each mode. The numerical value of T for each T_{90} is summarized in Table 1. T in Table 1 is the average value of those of related acoustic modes. Also listed in Table 1 are the difference between T and T_{90}, $(T-T_{90})$ and its uncertainty, $u(T-T_{90})$.

In Fig. 10c, the results obtained at the gallium melting point under the 'hung' configuration are compared with those under the 'sit' configuration. The T values obtained under the 'hung' configuration for various acoustic modes scattered within similar temperature range to those under the 'sit' configuration. This implies that under the present system, the difference between the 'hung' and 'sit' configurations was not significant. The results of the isotherm 293.15 K, as shown in Fig. 10b, seemed not to depend on the acoustic mode.

The uncertainty of $(T-T_{90})$, namely $u(T-T_{90})$, is mainly due to the contributions of temperature, pressure, microwave, and acoustic measurements. We estimated $u(T-T_{90})$ based on the categories and components as listed in Table 2. The uncertainty of the pressure measurements affects both the microwave and acoustic measurements, so it is included in both the microwave and acoustic categories.

The uncertainty related to the determination of T_{90} is the combination of several contributions from the cSPRTs and the imperfect temperature uniformity and

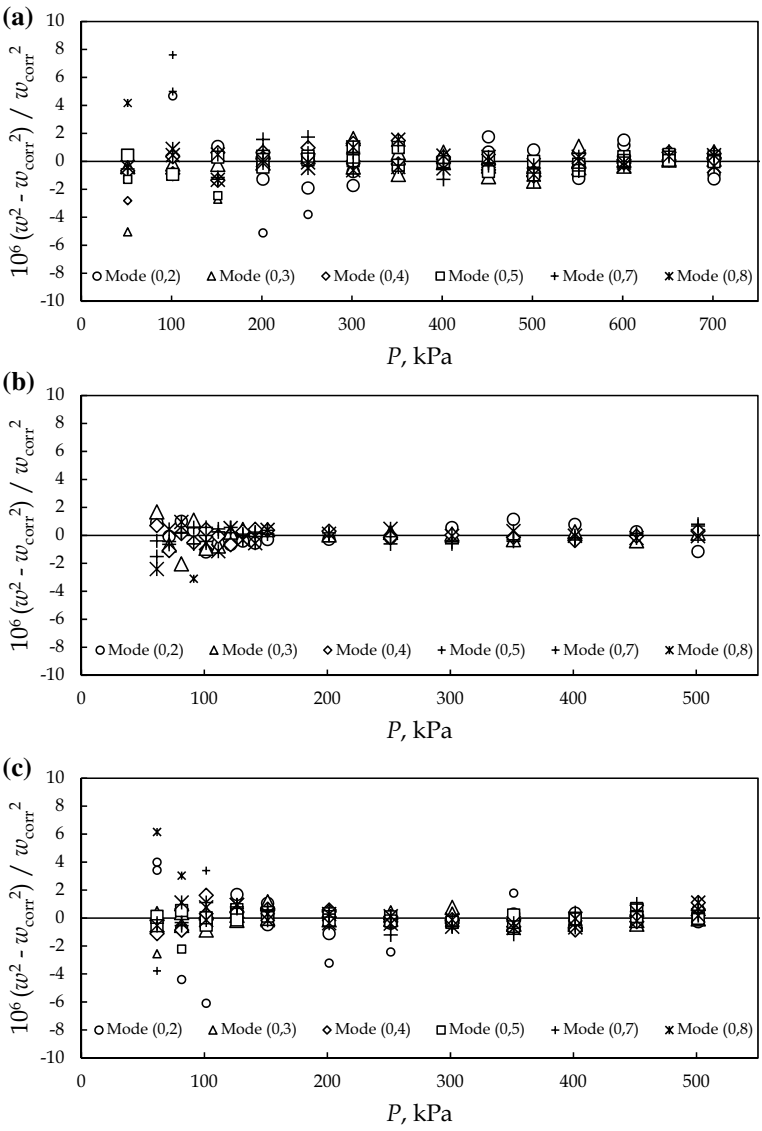

Fig. 9 Residual speed of sound: (**a**) at 273.16 K under 'Hung' configuration, (**b**) at 302.91 K under 'Hung' configuration, (**c**) at 273.16 K under 'Sit' configuration, (**d**) at 283.15 K under 'Sit' configuration, (**e**) at 293.15 K under 'Sit' configuration, (**f**) at 302.91 K under 'Sit' configuration; small-sized symbols for data excluded in fitting

stability of the cavity within the QSR. The uncertainty of the cSPRTs includes the calibration uncertainty at the TPW and at the gallium melting point, the long-term stability, which was estimated from the change in the resistance at the TPW, and the non-uniqueness. The non-uniqueness was estimated following the report by White and Strouse [25] and White et al. [26]. The uncertainty of the temperature realization within the QSR is the combination of the stability of temperature realized and

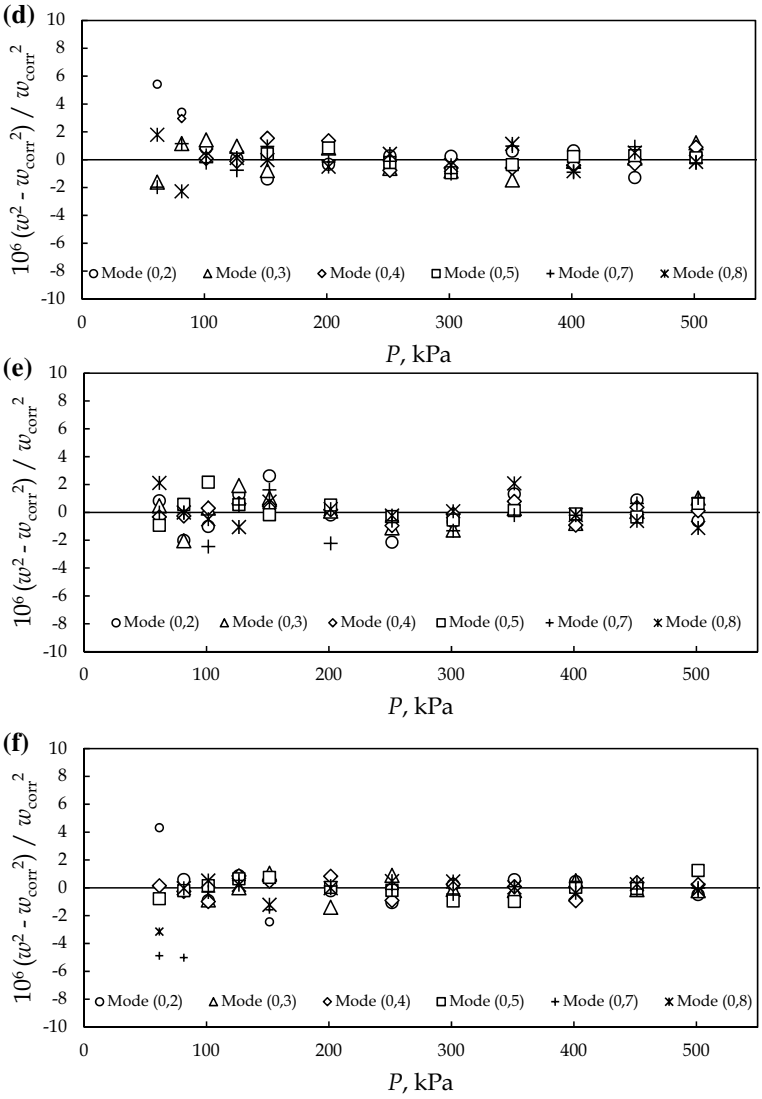

Fig. 9 (continued)

the temperature inhomogeneity across the QSR. Figure 11 represents the temperature measured by four cSPRTs, described in Sect. 2.3, under the 'hung' position and the 'sit' position. As shown in Fig. 11, the effect of heating from the pre-amplifier, attached at the south end microphone, in the 'hung' configuration was not satisfactorily compensated, resulting in a temperature inhomogeneity across the QSR within ± 0.6 mK. On the other hand, in the 'sit' configuration, the effect of heating from the pre-amplifier was satisfactorily compensated and the temperature of the QSR was uniform within ± 0.3 mK.

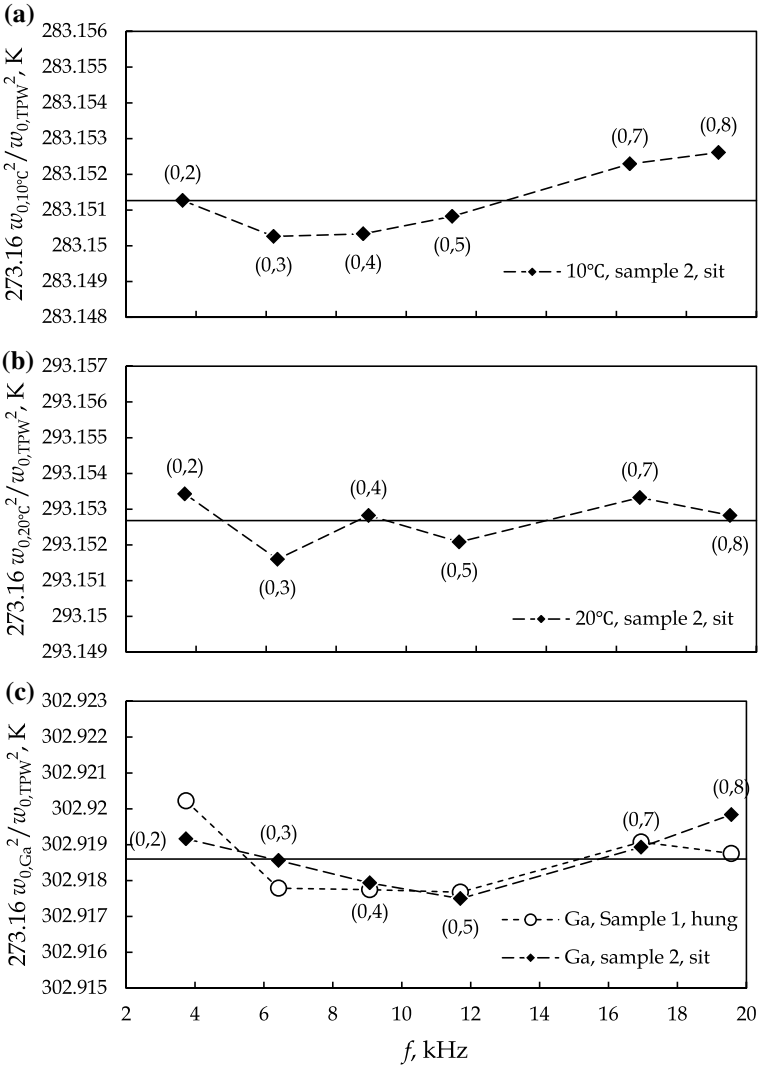

Fig. 10 Thermodynamic temperatures at various modes: (**a**) at 283.15 K, (**b**) at 293.15 K, (**c**) at 302.91 K

Table 1 Results of $(T-T_{90})$

T_{90}, K	T, K	$(T-T_{90})$, mK	$u(T-T_{90})$, mK
283.15	283.15127[a]	1.3	0.7
293.15	293.15268[a]	2.7	0.8
302.9146	302.91865[a]	4.1	0.8
302.9146	302.91854[b]	3.9	0.9

[a] 'sit' position

[b] 'hung' position

Table 2 Estimated uncertainty of $(T-T_{90})$

Category	Contribution, mK			
Component	283.2 K[a]	293.2 K[a]	302.9146 K[a]	302.9146 K[b]
Determination of T_{90}				
cSPRT long-term drift	0.08	0.08	0.08	0.08
TPW determination	0.21	0.21	0.21	0.21
cSPRT calibration	0.37	0.37	0.37	0.37
Temperature inhomogeneity of the resonator	0.17	0.17	0.17	0.35
Temperature stability	0.02	0.02	0.02	0.02
Non-uniqueness	0.11	0.20	0.28	0.28
Microwave measurements				
Mode inconsistency	0.07	0.07	0.07	0.07
Pressure	0.03	0.03	0.03	0.03
Acoustic measurements				
Acoustic measurements at TPW	0.04	0.04	0.04	0.06
Mode inconsistency at TPW	0.45	0.47	0.48	0.61
Acoustic measurements at T	0.09	0.12	0.07	0.06
Mode inconsistency at T	0.19	0.36	0.29	0.30
Pressure	0.03	0.03	0.03	0.03
Thermal accommodation	0.03	0.06	0.04	0.04
Combined uncertainty	0.7	0.8	0.8	0.9

[a] 'sit' position

[b] 'hung' position

The uncertainty related to the microwave measurements includes the mode inconsistency, the observed deviation of the thermal expansion, and compression of the radius from the calculations of the simplified model in Eq. 2 and the uncertainty of pressure measurement propagated to the microwave resonance frequency. The mode inconsistency was estimated from the discrepancy of a of the modes TM12 to TM14 and TE12 to TE13, represented in Fig. 5, from the average of a. This component may relate to effects that have not been completely compensated, namely a possible oxide layer on the inner surface of the QSR, slits, grooves, and holes formed due to misalignment of microphones, antennas, and hemispheres. Concerning the deviations of the effective radius from Eq. 2, these effects were included in the uncertainty for the acoustic measurements, so it is not listed in Table 2. The pressure effect was estimated based on the observed variation of the resonance frequency caused by the variation of the argon gas flow.

The uncertainty of our speed of sound determinations was combined from the acoustic frequency measurements at both TPW and T, including the mode discrepancy and the fitting uncertainty of the virial expansion for extrapolating to the limit zero pressure. Residuals from these fits are shown in Fig. 9, while the contribution from the discrepancies among different modes was calculated based on the speed of sound extrapolated to the limit zero pressure, w_0^2 in Eq. 4, for various acoustic modes. As in the case of microwave measurements, the effect of pressure

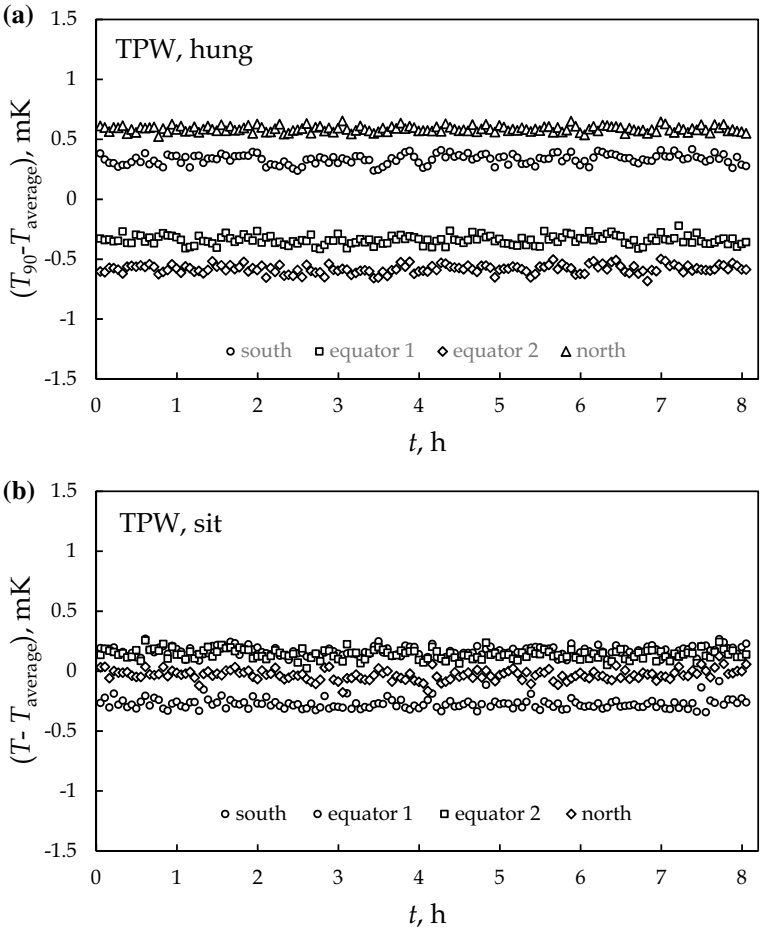

Fig. 11 Temperature stability and uniformity across the resonator at the TPW: (**a**) 'Hung' configuration, (**b**) 'Sit' configuration

measurements on the uncertainty of the acoustic measurements was estimated based on the difference in resonance frequency with and without argon gas flow.

In Sect. 3.2, it has been already stated that $h=1$ was used for the thermal accommodation parameter in this work. Using the assessment method of the coefficient h proposed in [22], we found h in the present system would be in the range between 0.7 and 1. Therefore, we consider the uncertainty due to h selection by comparing the case of $h=1$ and $h=0.7$.

The values of $(T-T_{90})$ listed in Table 1 exist in an overlapping temperature range including those reported by Moldover et al. [4], Ewing and Trusler [5], Benedetto et al. [6], Underwood et al. [9] and Gavioso et al. [10]. Figure 12 is a plot of these reported data in a range covering our results. The error bars show the standard uncertainty of each data. To make a better view, the error bar for the uncertainty in Table 1 is arrowed. It is seen from Fig. 12 that T at the gallium melting point agrees within

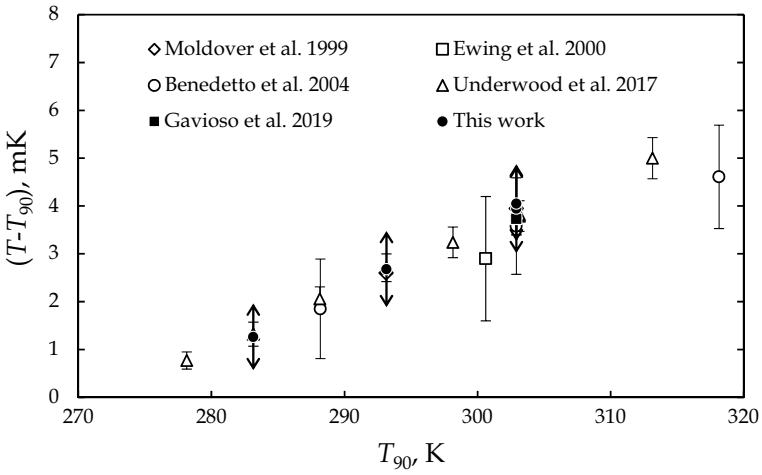

Fig. 12 Existing $(T-T_{90})$ and the present work

the estimated uncertainty with the data reported in [4, 5, 6, 9, 10]. T corresponding to $T_{90}=283.15$ K and $T_{90}=293.15$ K are both larger than those by Moldover et al. [3] and by Underwood et al. [9]. These differences are within the estimated uncertainty.

4 Conclusions

A new acoustic gas thermometry (AGT) system was built based on a diamond-turn QSR, where two different configurations for fixing the QSR were evaluated based on the measurement of the speed of sound in argon at the triple point of water and the melting point of gallium under the pressure range from 700 kPa down to 50 kPa. It was found from the thermodynamic temperatures obtained from these speed of sound measurements at the melting point of gallium that different QSR fixing configurations exhibit no significant difference to the value of the thermodynamic temperature determined. The speed of sound measurements at the isotherm of 283.15 K, 293.15 K, and 302.9146 K was also conducted and compared with the currently reported values that exist in overlapping temperature range with the present work. No significant difference was found between the present results and the reported values. They were in agreement within the estimated uncertainty.

Acknowledgments We would like to thank L. Pitre from LNE-CNAM, France; K. Gillis and M. R. Moldover from NIST, USA; and R. M. Gavioso from INRIM, Italy for sharing their vast knowledge and experiences, Y. Kano and K. Yamazawa from NMIJ for numerous technical discussions and many kinds of support. This study was partly supported by JSPS KAKENHI Grant Number 18K04189.

Appendix

See Table 3.

Table 3 Speed of sound of argon obtained in the present work

Hung, Sample 1											
T_{90} = 273.16 K											
Mode (0,2)		Mode (0,3)		Mode (0,4)		Mode (0,5)		Mode (0,7)		Mode (0,8)	
P, kPa	w^2, $m^2 \cdot s^{-2}$	P, kPa	w^2, $m^2 \cdot s^{-2}$	P, kPa	w^2, $m^2 \cdot s^{-2}$	P, kPa	w^2, $m^2 \cdot s^{-2}$	P, kPa	w^2, $m^2 \cdot s^{-2}$	P, kPa	w^2, $m^2 \cdot s^{-2}$
701.426	94 936.625	701.426	94 944.291	701.426	94 943.880	701.426	94 950.432	701.426	94 934.140	701.426	94 939.185
701.427	94 936.593	701.427	94 944.241	701.427	94 943.852	701.427	94 950.399	701.427	94 934.136	701.427	94 939.112
651.423	94 921.842	651.423	94 929.305	651.423	94 928.887	651.423	94 935.016	651.423	94 919.770	651.423	94 924.429
651.423	94 921.832	651.423	94 929.313	651.423	94 928.939	651.423	94 934.976	651.423	94 919.792	601.413	94 909.883
601.413	94 907.299	601.413	94 914.576	601.413	94 914.169	601.413	94 919.823	601.413	94 905.609	601.413	94 909.905
601.413	94 907.333	601.413	94 914.617	601.413	94 914.189	601.413	94 919.797	601.413	94 905.642	551.410	94 895.701
551.410	94 892.787	551.410	94 900.122	551.410	94 899.697	551.410	94 904.851	551.410	94 891.716	551.407	94 895.731
551.407	94 892.884	551.407	94 900.267	551.407	94 899.688	551.407	94 904.806	551.407	94 891.696	501.394	94 881.722
501.394	94 879.004	501.394	94 885.906	501.394	94 885.461	501.394	94 890.198	501.394	94 878.087	501.399	94 881.660
501.399	94 878.917	501.399	94 885.830	501.399	94 885.443	501.399	94 890.108	501.399	94 878.036	451.387	94 868.067
451.387	94 865.431	451.387	94 871.971	451.387	94 871.578	451.387	94 875.810	451.387	94 864.818	451.396	94 868.096
451.396	94 865.330	451.396	94 871.901	451.396	94 871.544	451.396	94 875.715	451.396	94 864.802	401.384	94 854.596
401.384	94 851.932	401.384	94 858.275	401.384	94 857.896	401.384	94 861.609	401.384	94 851.625	401.384	94 854.683
401.384	94 851.923	401.384	94 858.345	401.384	94 857.936	401.384	94 861.615	401.384	94 851.733	351.373	94 841.446
351.373	94 838.858	351.373	94 844.713	351.373	94 844.444	351.373	94 847.675	351.373	94 838.893	351.370	94 841.631
351.370	94 838.819	351.370	94 844.858	351.370	94 844.602	351.370	94 847.795	351.370	94 839.024	301.375	94 828.529
301.375	94 825.986	301.375	94 831.523	301.375	94 831.267	301.375	94 834.043	301.375	94 826.334	301.367	94 828.682
301.367	94 826.079	301.367	94 831.713	301.367	94 831.387	301.367	94 834.134	301.367	94 826.404	251.353	94 815.904
251.356	94 813.546	251.353	94 818.582	251.353	94 818.362	251.353	94 820.628	251.353	94 814.075	251.356	94 815.942
201.356	94 801.495	251.356	94 818.597	251.356	94 818.405	251.356	94 820.654	251.356	94 814.185	201.354	94 803.581
151.354	94 789.912	201.354	94 805.844	201.354	94 805.669	201.354	94 807.462	201.354	94 802.097	201.356	94 803.563
101.374	94 778.439	201.356	94 805.769	201.356	94 805.630	201.356	94 807.411	201.356	94 802.024	151.354	94 791.502

Table 3 (continued)

Hung, Sample 1											
T_{90} = 273.16 K											
Mode (0,2)		Mode (0,3)		Mode (0,4)		Mode (0,5)		Mode (0,7)		Mode (0,8)	
P, kPa	w^2, $m^2 \cdot s^{-2}$	P, kPa	w^2, $m^2 \cdot s^{-2}$	P, kPa	w^2, $m^2 \cdot s^{-2}$	P, kPa	w^2, $m^2 \cdot s^{-2}$	P, kPa	w^2, $m^2 \cdot s^{-2}$	P, kPa	w^2, $m^2 \cdot s^{-2}$
		151.354	94 793.226	151.354	94 793.206	151.354	94 794.556	151.354	94 790.008	151.352	94 791.329
		101.350	94 780.926	151.352	94 793.018	101.350	94 781.761	151.352	94 790.019	101.350	94 779.678
		101.374	94 780.947	101.350	94 780.959	101.374	94 781.822	51.358	94 767.183	101.374	94 779.641
		51.358	94 768.842	101.374	94 780.849	51.358	94 769.459	51.396	94 767.220	51.396	94 767.959
				51.396	94 768.898						
Hung, Sample 1											
T_{90} = 302.9146 K											
Mode (0,2)		Mode (0,3)		Mode (0,4)		Mode (0,5)		Mode (0,7)		Mode (0,8)	
P, kPa	w^2, $m^2 \cdot s^{-2}$	P, kPa	w^2, $m^2 \cdot s^{-2}$	P, kPa	w^2, $m^2 \cdot s^{-2}$	P, kPa	w^2, $m^2 \cdot s^{-2}$	P, kPa	w^2, $m^2 \cdot s^{-2}$	P, kPa	w^2, $m^2 \cdot s^{-2}$
501.393	105 349.993	501.393	105 357.366	501.393	105 356.587	501.393	105 361.173	501.393	105 350.535	501.393	105 353.147
451.416	105 321.686	451.416	105 328.694	451.416	105 328.023	451.416	105 332.083	451.416	105 322.405	451.416	105 324.749
401.379	105 293.579	401.379	105 300.316	401.379	105 299.634	401.379	105 303.206	401.379	105 294.497	401.379	105 296.590
351.389	105 265.810	351.389	105 272.039	351.389	105 271.534	351.389	105 274.594	351.389	105 266.856	351.389	105 268.718
301.381	105 238.255	301.381	105 244.057	301.381	105 243.622	301.381	105 246.190	301.381	105 239.412	301.381	105 241.008
251.386	105 211.020	251.386	105 216.255	251.386	105 215.886	251.386	105 218.052	251.386	105 212.224	251.386	105 213.636
201.386	105 184.171	201.386	105 188.622	201.386	105 188.418	201.386	105 190.093	201.386	105 185.338	201.386	105 186.411
151.374	105 157.651	151.374	105 161.241	151.374	105 161.104	151.374	105 162.367	151.374	105 158.573	151.374	105 159.488
141.383	105 152.365	141.383	105 155.788	141.383	105 155.678	141.383	105 156.832	141.383	105 153.260	141.383	105 154.033
131.384	105 147.131	131.384	105 150.338	131.384	105 150.232	131.384	105 151.301	131.384	105 147.930	131.384	105 148.708

Table 3 (continued)

Hung, Sample 1											
T_{90} = 302.9146 K											
Mode (0,2)		Mode (0,3)		Mode (0,4)		Mode (0,5)		Mode (0,7)		Mode (0,8)	
P, kPa	w^2, $m^2 \cdot s^{-2}$	P, kPa	w^2, $m^2 \cdot s^{-2}$	P, kPa	w^2, $m^2 \cdot s^{-2}$	P, kPa	w^2, $m^2 \cdot s^{-2}$	P, kPa	w^2, $m^2 \cdot s^{-2}$	P, kPa	w^2, $m^2 \cdot s^{-2}$
121.377	105 141.864	121.377	105 144.871	121.377	105 144.707	121.377	105 145.799	121.377	105 142.681	121.377	105 143.452
111.374	105 136.647	111.374	105 139.331	111.374	105 139.356	111.374	105 140.326	111.374	105 137.349	111.374	105 137.945
101.388	105 131.378	101.388	105 133.895	101.388	105 134.009	101.388	105 134.747	101.388	105 132.102	101.388	105 132.691
91.391	105 126.344	91.391	105 128.690	91.391	105 128.513	91.391	105 129.368	91.391	105 126.699	81.391	105 122.236
81.391	105 121.227	81.391	105 122.950	81.391	105 123.191	81.391	105 123.856	81.391	105 121.509	71.391	105 116.888
71.391	105 115.941	71.391	105 117.690	71.391	105 117.682	71.391	105 118.300	71.391	105 116.184		
61.387	105 110.886	61.387	105 112.543	61.387	105 112.495	61.387	105 112.867				
Sit, Sample 2											
T_{90} = 273.16 K											
Mode (0,2)		Mode (0,3)		Mode (0,4)		Mode (0,5)		Mode (0,7)		Mode (0,8)	
P, kPa	w^2, $m^2 \cdot s^{-2}$	P, kPa	w^2, $m^2 \cdot s^{-2}$	P, kPa	w^2, $m^2 \cdot s^{-2}$	P, kPa	w^2, $m^2 \cdot s^{-2}$	P, kPa	w^2, $m^2 \cdot s^{-2}$	P, kPa	w^2, $m^2 \cdot s^{-2}$
501.509	94 879.032	501.509	94 885.787	501.509	94 885.612	501.509	94 889.836	501.509	94 879.692	501.509	94 881.776
501.498	94 878.964	501.498	94 885.888	501.498	94 885.522	501.498	94 889.836	501.498	94 879.710	501.498	94 881.685
451.501	94 865.280	451.501	94 871.831	451.501	94 871.606	451.501	94 875.519	451.501	94 866.310	451.501	94 868.088
451.492	94 865.229	451.492	94 871.853	451.492	94 871.566	451.492	94 875.462	451.492	94 866.257	451.492	94 868.024
401.496	94 851.866	401.496	94 858.136	401.496	94 857.851	401.496	94 861.314	401.496	94 853.048	401.496	94 854.658
401.486	94 851.906	401.486	94 858.153	401.486	94 857.831	401.486	94 861.307	401.486	94 852.960	401.486	94 854.597
351.480	94 838.834	351.493	94 844.672	351.493	94 844.457	351.493	94 847.366	351.493	94 839.940	351.493	94 841.484
301.489	94 826.062	351.480	94 844.669	351.480	94 844.408	351.480	94 847.438	351.480	94 839.978	351.480	94 841.448

Table 3 (continued)

Sit, Sample 2											
T_{90} = 273.16 K											
Mode (0,2)		Mode (0,3)		Mode (0,4)		Mode (0,5)		Mode (0,7)		Mode (0,8)	
P, kPa	w^2, $m^2 \cdot s^{-2}$	P, kPa	w^2, $m^2 \cdot s^{-2}$	P, kPa	w^2, $m^2 \cdot s^{-2}$	P, kPa	w^2, $m^2 \cdot s^{-2}$	P, kPa	w^2, $m^2 \cdot s^{-2}$	P, kPa	w^2, $m^2 \cdot s^{-2}$
301.478	94 826.068	301.489	94 831.547	301.489	94 831.223	301.489	94 833.740	301.489	94 827.268	301.489	94 828.603
251.477	94 813.619	301.478	94 831.497	301.478	94 831.242	301.478	94 833.738	301.478	94 827.271	301.478	94 828.553
201.491	94 801.464	251.489	94 818.496	251.489	94 818.252	251.489	94 820.368	251.489	94 814.840	251.489	94 815.960
151.498	94 789.903	251.477	94 818.448	251.477	94 818.282	251.477	94 820.338	251.477	94 814.726	251.477	94 815.907
151.487	94 789.756	201.491	94 805.721	201.491	94 805.581	201.491	94 807.223	201.491	94 802.606	201.491	94 803.484
126.475	94 784.076	201.477	94 805.655	201.477	94 805.566	201.477	94 807.177	201.477	94 802.645	201.477	94 803.542
126.492	94 784.200	151.487	94 793.098	151.498	94 793.060	151.498	94 794.305	151.498	94 790.635	151.498	94 791.355
101.499	94 778.307	126.475	94 786.881	151.487	94 793.065	151.487	94 794.278	151.487	94 790.643	151.487	94 791.308
81.521	94 773.806	126.492	94 786.919	126.475	94 786.865	126.475	94 787.945	126.475	94 784.746	126.475	94 785.401
		101.513	94 780.796	126.492	94 786.835	126.492	94 787.880	126.492	94 784.739	126.492	94 785.404
		101.499	94 780.676	101.513	94 780.872	101.513	94 781.534	101.513	94 778.927	101.513	94 779.357
		81.521	94 775.836	101.499	94 780.716	101.499	94 781.581	81.521	94 774.128	101.499	94 779.438
		81.511	94 775.921	81.521	94 775.784	81.511	94 776.624	81.511	94 774.147	81.511	94 774.756
		61.523	94 771.075	81.511	94 775.916	61.535	94 771.620	61.523	94 769.539	61.535	94 769.924
				61.535	94 770.960	61.523	94 771.553				
				61.523	94 770.944						

Table 3 (continued)

Sit, Sample 2											
T_{90} = 283.15 K											
Mode (0,2)		Mode (0,3)		Mode (0,4)		Mode (0,5)		Mode (0,7)		Mode (0,8)	
P, kPa	w^2, $m^2 \cdot s^{-2}$	P, kPa	w^2, $m^2 \cdot s^{-2}$	P, kPa	w^2, $m^2 \cdot s^{-2}$	P, kPa	w^2, $m^2 \cdot s^{-2}$	P, kPa	w^2, $m^2 \cdot s^{-2}$	P, kPa	w^2, $m^2 \cdot s^{-2}$
501.488	98 399.448	501.488	98 406.306	501.488	98 406.099	501.488	98 409.172	501.488	98 401.122	501.488	98 402.145
451.487	98 380.110	451.487	98 386.947	451.487	98 386.687	451.487	98 389.513	451.487	98 382.230	451.487	98 383.112
401.481	98 361.454	401.481	98 367.868	401.481	98 367.592	401.481	98 370.063	401.481	98 363.295	401.481	98 364.137
351.479	98 342.938	351.479	98 348.875	351.479	98 348.704	351.479	98 350.795	351.479	98 344.976	351.479	98 345.744
301.483	98 324.720	301.483	98 330.277	301.483	98 330.045	301.483	98 331.760	301.483	98 326.531	301.483	98 327.263
251.477	98 306.864	251.477	98 311.821	251.477	98 311.575	251.477	98 313.083	251.477	98 308.614	251.477	98 309.262
201.478	98 289.276	201.478	98 293.687	201.478	98 293.544	201.478	98 294.667	201.478	98 290.855	201.478	98 291.347
151.508	98 271.980	151.508	98 275.452	151.508	98 275.538	151.508	98 276.347	151.508	98 273.469	151.508	98 273.831
126.494	98 263.641	126.494	98 266.648	126.494	98 266.431	101.501	98 258.283	126.494	98 264.635	126.494	98 265.149
101.501	98 255.319	101.501	98 257.772	101.501	98 257.566	61.526	98 243.885	101.501	98 256.092	101.501	98 256.540
		81.511	98 250.644	61.526	98 243.379			81.511	98 249.395	81.511	98 249.431
		61.526	98 243.303					61.526	98 242.299	61.526	98 243.017
Sit, Sample 2											
T_{90} = 293.15 K											
Mode (0,2)		Mode (0,3)		Mode (0,4)		Mode (0,5)		Mode (0,7)		Mode (0,8)	
P, kPa	w^2, $m^2 \cdot s^{-2}$	P, kPa	w^2, $m^2 \cdot s^{-2}$	P, kPa	w^2, $m^2 \cdot s^{-2}$	P, kPa	w^2, $m^2 \cdot s^{-2}$	P, kPa	w^2, $m^2 \cdot s^{-2}$	P, kPa	w^2, $m^2 \cdot s^{-2}$
501.491	101 918.137	501.491	101 925.235	501.491	101 924.864	501.491	101 927.944	501.491	101 919.366	501.491	101 920.671
451.488	101 894.242	451.488	101 900.955	451.488	101 900.667	451.488	101 903.288	451.488	101 895.583	451.488	101 896.751
401.483	101 870.396	401.483	101 876.877	401.483	101 876.534	401.483	101 878.977	401.483	101 871.973	401.483	101 873.060

Table 3 (continued)

Sit, Sample 2											
T_{90} = 293.15 K											
Mode (0,2)		Mode (0,3)		Mode (0,4)		Mode (0,5)		Mode (0,7)		Mode (0,8)	
P, kPa	w^2, $m^2 \cdot s^{-2}$	P, kPa	w^2, $m^2 \cdot s^{-2}$	P, kPa	w^2, $m^2 \cdot s^{-2}$	P, kPa	w^2, $m^2 \cdot s^{-2}$	P, kPa	w^2, $m^2 \cdot s^{-2}$	P, kPa	w^2, $m^2 \cdot s^{-2}$
351.377	101 847.112	351.377	101 853.139	351.377	101 852.873	351.377	101 854.840	351.377	101 848.623	351.377	101 849.745
301.477	101 823.879	301.477	101 829.424	301.477	101 829.263	301.477	101 830.930	301.477	101 825.474	301.477	101 826.329
251.475	101 800.972	251.475	101 806.025	251.475	101 805.829	251.475	101 807.285	251.475	101 802.684	251.475	101 803.273
201.480	101 778.741	201.480	101 782.926	201.480	101 782.816	201.480	101 783.926	201.480	101 779.877	201.480	101 780.536
151.488	101 756.918	151.488	101 759.991	151.488	101 759.930	151.488	101 760.631	151.488	101 757.846	151.488	101 758.043
126.496	101 745.848	126.496	101 748.639	126.496	101 748.575	126.496	101 749.177	126.496	101 746.608	126.496	101 746.672
101.506	101 734.763	101.506	101 737.080	101.506	101 737.223	81.517	101 728.570	101.506	101 735.231	101.506	101 735.604
81.517	101 726.038	81.517	101 727.761	81.517	101 728.151	61.533	101 719.316	81.517	101 726.661	81.517	101 726.797
61.533	101 717.758	61.533	101 718.969	61.533	101 719.165			61.533	101 717.881	61.533	101 718.195
Sit, Sample 2											
T_{90} = 302.9146 K											
Mode (0,2)		Mode (0,3)		Mode (0,4)		Mode (0,5)		Mode (0,7)		Mode (0,8)	
P, kPa	w^2, $m^2 \cdot s^{-2}$	P, kPa	w^2, $m^2 \cdot s^{-2}$	P, kPa	w^2, $m^2 \cdot s^{-2}$	P, kPa	w^2, $m^2 \cdot s^{-2}$	P, kPa	w^2, $m^2 \cdot s^{-2}$	P, kPa	w^2, $m^2 \cdot s^{-2}$
501.494	105 350.092	501.494	105 357.102	501.494	105 356.976	501.494	105 360.291	501.494	105 351.452	501.494	105 353.339
451.490	105 321.726	451.490	105 328.484	451.490	105 328.404	451.490	105 331.180	451.490	105 323.244	451.490	105 324.930
401.488	105 293.631	401.488	105 300.133	401.488	105 299.880	401.488	105 302.427	401.488	105 295.315	401.488	105 296.659
351.484	105 265.841	351.484	105 271.843	351.484	105 271.795	351.484	105 273.769	351.484	105 267.526	351.484	105 268.741
301.482	105 238.314	301.482	105 243.843	301.482	105 243.822	301.482	105 245.435	301.482	105 239.937	301.482	105 241.072
251.483	105 211.009	251.483	105 216.147	251.483	105 215.906	251.483	105 217.390	251.483	105 212.658	251.483	105 213.608

Table 3 (continued)

Sit, Sample 2											
T_{90} = 302.9146 K											
Mode (0,2)		Mode (0,3)		Mode (0,4)		Mode (0,5)		Mode (0,7)		Mode (0,8)	
P, kPa	w^2, $m^2 \cdot s^{-2}$	P, kPa	w^2, $m^2 \cdot s^{-2}$	P, kPa	w^2, $m^2 \cdot s^{-2}$	P, kPa	w^2, $m^2 \cdot s^{-2}$	P, kPa	w^2, $m^2 \cdot s^{-2}$	P, kPa	w^2, $m^2 \cdot s^{-2}$
201.487	105 184.244	201.487	105 188.311	201.487	105 188.495	201.487	105 189.500	201.487	105 185.592	201.487	105 186.335
126.505	105 144.673	151.497	105 161.179	151.497	105 161.063	151.497	105 161.877	126.505	105 145.415	151.497	105 159.239
101.516	105 131.416	126.505	105 147.452	126.505	105 147.480	126.505	105 148.098	101.516	105 132.034	126.505	105 145.998
81.528	105 121.179	101.516	105 133.796	101.516	105 133.714	101.516	105 134.331			101.516	105 132.700
		61.545	105 112.331	81.528	105 122.970	81.528	105 123.361			81.528	105 122.023
				61.545	105 112.225	61.545	105 112.404				

References

1. The International System of Units (SI), https://www.bipm.org/en/measurement-units/
2. M.R. Moldover, J.P.M. Trusler, T.J. Edwards, J. Res. Natl. Bur. Stand. **93**, 85 (1988)
3. M.R. Moldover, J.P.M. Trusler, Metrologia **25**, 165 (1988)
4. M.R. Moldover, S.J. Boyes, C.W. Meyer, A.R.H. Goodwin, J. Res. Natl. Bur. Stand. **104**, 11 (1999)
5. M.B. Ewing, J.P.M. Trusler, J. Chem. Thermodyn. **32**, 1229 (2000)
6. G. Benedetto, R.M. Gavioso, R. Spagnolo, P. Marcarino, A. Merlone, Metrologia **41**, 74 (2004)
7. L. Pitre, M.R. Moldover, W.L. Tew, Metrologia **43**, 142 (2006)
8. D.C. Ripple, G.F. Strouse, M.R. Moldover, Int. J. Thermophys. **28**, 1789 (2007)
9. R. Underwood, M. de Podesta, G. Sutton, L. Stanger, R. Rusby, P. Harris, P. Morantz, G. Machin, Int. J. Thermophys. **38**, 44 (2017)
10. R.M. Gavioso, D. Madonna Ripa, P.P.M. Steur, R. Dematteis, D. Imbraguglio, Metrologia **56**, 045006 (2019)
11. H. Preston-Thomas, Metrologia **27**, 3 (1990)
12. J. Fischer, M. de Podesta, K.D. Hill, M. Moldover, L. Pitre, R. Rusby, P. Steur, O. Tamura, R. White, L. Wolber, Int. J. Thermophys. **32**, 12 (2011)
13. T. Misawa, J. Widiatmo, Y. Kano, T. Sasagawa, K. Yamazawa, Int. J. Thermophys. **39**, 4 (2018)
14. R. Underwood, D. Flack, P. Morantz, G. Sutton, P. Shore, M. de Podesta, Metrologia **48**, 1 (2011)
15. J.B. Mehl, M.R. Moldover, L. Pitre, Metrologia **41**, 295 (2004)
16. T. Nakano, I. Saito, Y. Kawamura, J. V. Widiatmo, in Proc. SICE Annual Conference, September 2018, Nara, Japan
17. Mise en Pratique for the Definition of the kelvin in the SI, SI Brochure—9th edition (2019)—Appendix 2, https://www.bipm.org/utils/en/pdf/si-mep/SI-App2-kelvin.pdf
18. M.R. Moldover, R.M. Gavioso, J.B. Mehl, L. Pitre, M. de Podesta, Z.T. Zhang, Metrologia **51**, R1–R19 (2014)
19. J.B. Mehl, Metrologia **52**, S227 (2015)
20. G. Sutton, R. Underwood, L. Pitre, M. de Podesta, S. Valkiers, Int. J. Thermophys. **31**, 1310 (2010)
21. K.A. Gillis, H. Lin, M.R. Moldover, J. Res. Natl. Inst. Stand. Technol. **114**, 263 (2009)
22. L. Pitre, F. Sparasci, D. Truong, A. Guillou, L. Risegari, M. Himbert, Int. J. Thermophys. **32**, 1825 (2011)
23. M.B. Ewing, A.R.H. Goodwin, J. Chem. Thermodyn. **24**, 531 (1992)
24. D.B. Newell, F. Cabiati, J. Fischer, K. Fujii, S.G. Karshenboim, H.S. Margolis, E. de Mirandés, P.J. Mohr, F. Nez, K. Pachucki, T.J. Quinn, B.N. Taylor, M. Wang, B.M. Wood, Z. Zhang, Metrologia **55**, L13 (2018)
25. D.R. White, G.F. Strouse, Metrologia **46**, 101 (2009)
26. D. R. White, M. Ballico, V. Chimenti, S. Duris, E. Filipe, A. Ivanova, A. Kartal Dogan, E. Mendez-Lango, C. Meyer, F. Pavese, A. Peruzzi, E. Renaot, S. Rudtsch, K. Yamazawa, CCT-WG3 on uncertainty in contact thermometry, July 2009

Publisher's Note Springer Nature remains neutral with regard to jurisdictional claims in published maps and institutional affiliations.